AGU PUBLICATIONS

JGR

Journal of Geophysical Research: Solid Earth

RESEARCH ARTICLE

10.1002/2013JB010932

**Key Points:**
- Location of coseismic and postseismic changes at different depth
- Significant loading effects of the rain at depth
- Imaging procedure based on the sensitivity of scattered waves to weak changes

**Correspondence to:**
A. Obermann,
anne_obermann@yahoo.de

**Citation:**
Obermann, A., B. Froment, M. Campillo, E. Larose, T. Planès, B. Valette, J. H. Chen, and Q. Y. Liu (2014), Seismic noise correlations to image structural and mechanical changes associated with the *Mw* 7.9 2008 Wenchuan earthquake, *J. Geophys. Res. Solid Earth*, *119*, doi:10.1002/2013JB010932.

Received 29 DEC 2013
Accepted 9 MAR 2014
Accepted article online 15 MAR 2014

# Seismic noise correlations to image structural and mechanical changes associated with the *Mw* 7.9 2008 Wenchuan earthquake

**A. Obermann[1], B. Froment[2], M. Campillo[1], E. Larose[1], T. Planès[1,3], B. Valette[4], J. H. Chen[5], and Q. Y. Liu[5]**

[1]ISTerre, Université Joseph Fourier, Grenoble, CEDEX 9, France, [2]Earth Resources Laboratory, Massachusetts Institute of Technology, Cambridge, Massachusetts, USA, [3]Department of Civil and Environmental Engineering, Colorado School of Mines Golden, Colorado, USA, [4]ISTerre, IRD, Université de Savoie, Le Bourget-du-Lac, CEDEX, France, [5]State Key Laboratory of Earthquake Dynamics, Institute of Geology, China Earthquake Administration, Beijing, China

**Abstract** We locate temporal changes of seismic wave speed and scattering properties of the crust associated with the 2008 *Mw* 7.9 Wenchuan earthquake. To that end, we analyze ambient seismic noise records from 2007 until the end of 2008 in the 1–3 s period band and in the 12–20 s period band measured in a region that covers the southern two thirds of the fault activated during the earthquake. To locate the changes, we use a refined imaging procedure based on the sensitivity of scattered waves to weak perturbations. This inverse method uses the radiative transfer approximation to describe the intensity of the noise correlation coda. Our results show that the largest structural changes are observed northeast of the Wenchuan epicenter, around the fault zone where aftershocks are distributed. The spatial and temporal characteristics of the behavior of the crust at depth around the Wenchuan earthquake suggest a postseismic and geology-dependent signature of the middle crust. We also observe a clear seasonal signature within the Sichuan basin at depth that we relate to the heavy rainfalls during the monsoon season. This seasonality can also be observed at the surface in form of a waveform decoherence. Our study highlights that seismic velocity changes, and waveform decoherence are independent measurements that are sensitive to different parameters and can thus give complementary information. In our study we also point out the value of studying the evolution of the changes at different times in the coda.

## 1. Introduction

On 12 May 2008, a *Mw* 7.9 earthquake struck the Longmen Shan region, China, along the eastern margin of the Tibetan Plateau [*Burchfiel et al.*, 2008; *Zhang et al.*, 2010]. This earthquake caused over 80,000 fatalities and enormous material damage. Surface geological surveys indicate a 240 km long rupture zone [*Xu et al.*, 2009]. Nearly 300 strong aftershocks followed the main shock along the rupture zone [*Chen et al.*, 2009; *Fu et al.*, 2011] (red dots in Figure 2). The hypocenter was located at 14–19 km depth [*Chen et al.*, 2009].

In October 2006, the Institute of Geology of the China Earthquake Administration deployed about 300 broadband seismic stations in the Western Sichuan province. This Sichuan Seismic Array (WSSA) covers two thirds of the fault system activated during the Wenchuan earthquake in 2008. The network was operated continuously from the initial installation until the end of 2008 and provides unique recordings before, during, and after the Wenchuan quake. A collaboration agreement gave us access to the pretreated data (amplitude normalization, stack over 10 days) from January 2007 until December 2008 from the northern half of the array (Figure 2).

The physical processes that accompany earthquakes, such as coseismic stress changes, the migration of fluids, and the formation of damage zones in the shallow layers, are likely to cause changes in mechanical properties of nearby crustal material. The sensitivity of the multiply scattered coda of ambient seismic noise cross correlations is, in general, high enough to detect relative changes in the order of $10^{-4}$ [*Brenguier et al.*, 2008]. With the approximation that the sensitivity of coda waves at early times in the coda is dominated by surface waves, we can study the noise correlations in different frequency bands that are sensitive to different depths. In previous works, *Chen et al.* [2010] used this same data set and showed that they could track the temporal change of the seismic wave speed in the 1–3 s period band (sensitive to the upper crust) at a regional scale. They found clear evidence that the seismic velocity dropped by up to 0.08% in the fault region just after the earthquake with fluctuations within 0.02% prior to the earthquake. They split the area of

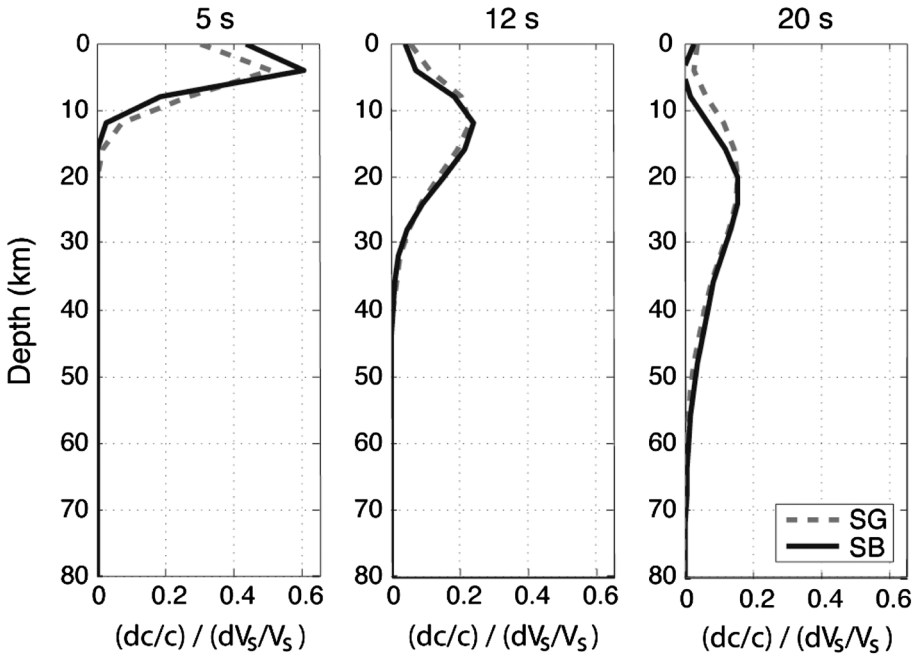


**Figure 1.** Depth sensitivity of the Rayleigh phase velocity $c$ to a shear wave velocity perturbation $dV_s$ at 5, 12, and 20 s computed in the region of interest (figure from *Froment et al.* [2013]). SG (grey-dashed line) corresponds to an analysis in the Songpan-Ganzi block and SB (black line) to the Sichuan basin.

interest in different subarrays and compared the measurements of these arrays to obtain a spatial distribution of the velocity changes. They found the distribution to be consistent with the volumetric strain change during the Wenchuan earthquake and could show that the coseismic velocity changes are not controlled by the response of the sediments.

Still using the same data subset, *Froment et al.* [2013] investigated the temporal changes of the seismic wave speed at larger depth. To do that, they used the 12–20 s period band, which has its maximum sensitivity for 20–30 km depth. Besides a velocity drop associated with the earthquake, they also detected apparent seasonal variations of the seismic velocity in the Sichuan basin. By comparison with measurements in the 1–3 s period band, they show that the seismic velocity changes in the 12–20 s period band cannot be explained by a shallow perturbation but are related to deformation at depth in the crust. They used these variations to characterize the middle crust behavior around the Wenchuan earthquake. Their results suggest that the deformation in the middle crust is different beneath Tibet and the Sichuan basin.

In the present paper we study the temporal changes of seismic wave speed and the distortion of the seismic waveform (waveform decoherence) due to structural changes in the medium in both the 1–3 s and 12–20 s period bands. We chose these frequencies, as in the 1–3 s period band the sensitivity of the Rayleigh phase velocity to a medium perturbation is limited to the upper 10 km, while the sensitivity in the 12–20 s period band is the highest between 10 and 30 km. We can hence separately investigate the shallow and middle crust. Figure 1 shows the depth sensitivities of the Rayleigh phase velocities computed by Huang and van der Hilst at 5, 12, and 20 s.

Based on recent results in wave physics [*Larose et al.*, 2010; *Rossetto et al.*, 2011; *Froment*, 2011; *Planès*, 2013; *Planès et al.*, 2014], we then use an imaging procedure [*Obermann et al.*, 2013a] that is based on the sensitivity of multiply scattered waves to weak changes in the medium and that allows spatial localization of changes in medium properties. With this method we can successfully image the lateral distribution of the velocity variations and the structural changes associated with the 2008 Wenchuan earthquake, as well as the heavy rainfalls in the monsoon season in summer 2007 and 2008. As *Obermann et al.* [2013b] pointed out the varying sensitivity of coda waves at different lapse times, we further develop the inversion technique to jointly invert for different times in the coda.

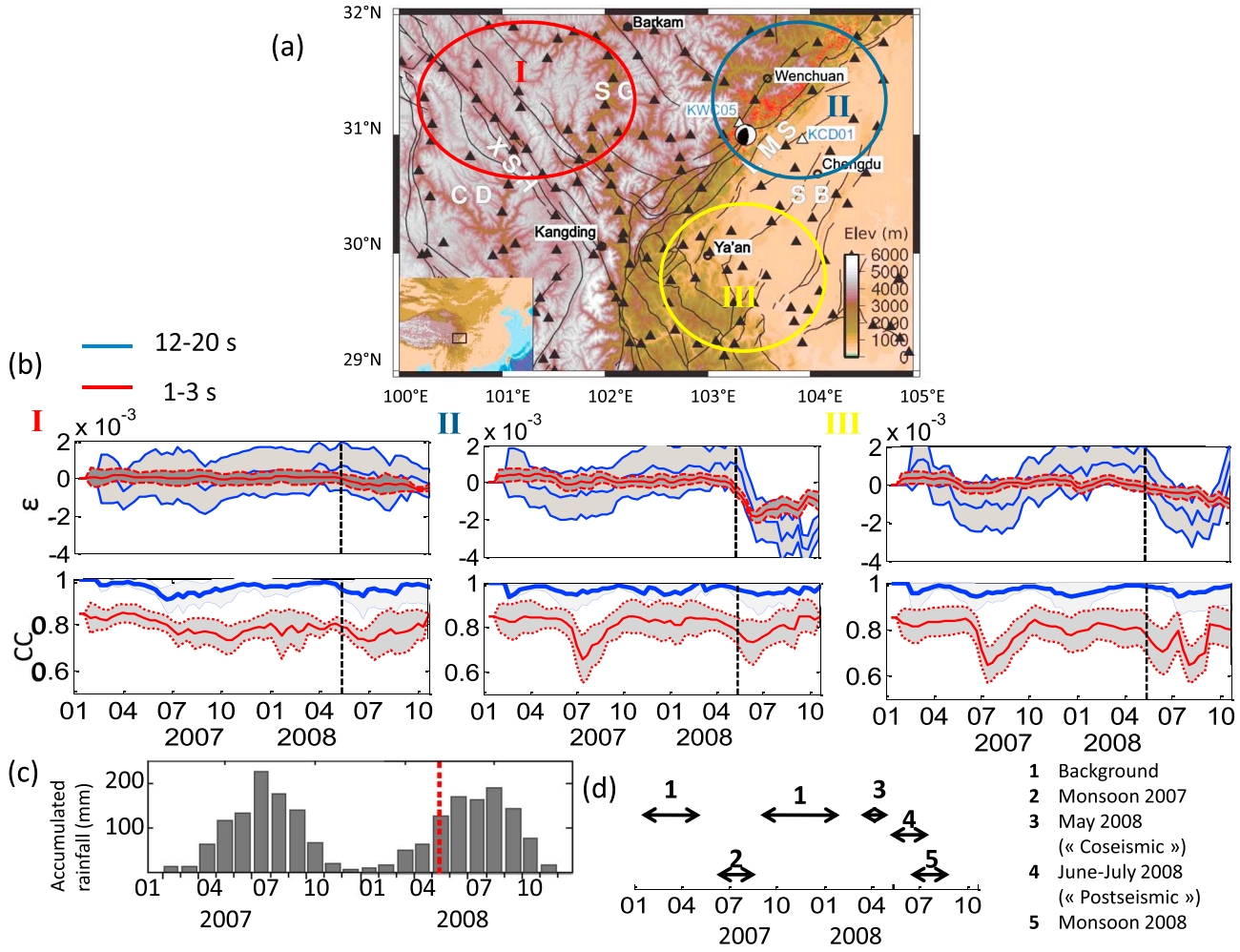


**Figure 2.** (a) Location map of the stations used in the present study (black triangles). The beach ball indicates the epicenter of the Wenchuan earthquake, and the red dots represent the aftershocks [*Chen et al.*, 2009]. The black lines show the major faults in the region. SB, SG, and LMS indicate the main geological units to which this study refers: the Sichuan sedimentary basin, the Songpan-Ganzi block, and the Longmen Shan fault zone, respectively. The colored circles indicate the subregions (I to III) for which we show the (b) velocity variations and the coherence with their respective error bars at 50 s in the coda: the Pre-Himalaya (red, I), the Longmen Shan region where the earthquake took place (blue, II), and the southern Sichuan basin (yellow, III). (c) The monthly accumulated rainfall in the Sichuan basin. (d) The time spans over which we averaged the delay times and coherence values (background state, July–August 2007 (peak of the monsoon), May 2008 (centered around the earthquake), June–July 2008 (shortly after the earthquake), and July–August 2008 (peak of the monsoon)) (figure inspired by *Froment et al.* [2013]).

In section 2, we describe the seismic data that we use in this study and briefly explain the computation of the cross-correlation functions. We then discuss the determination of the relative velocity changes and the decoherence with the stretching technique. In section 3, we explain the linear least squares inversion that we use to locate the medium changes. In section 4 we show and discuss the inversion results for the velocity changes and the waveform decoherence in the shallow and middle crust. We particularly emphasize that the apparent velocity changes and the waveform decoherence show different behavior at different times in the coda. We use this time evolution to obtain qualitative information at depth.

## 2. Seismic Data and Data Processing

The study area comprises the northern part of the WSSA (29° to 32°N and 100° to 105°E). In this area are 156 stations, with an average station spacing of 20 to 30 km. We remove stations with instrumental timing errors using a time symmetry argument for noise cross correlations as introduced by *Stehly et al.* [2007]. The remaining 114 stations are distributed over different geological units in this area (Figure 2): the Pre-Himalaya with the Songpan-Ganzi (SG) and Chuan-Dian (CD) blocks, the Longmen Shan mountain range (LMS), and

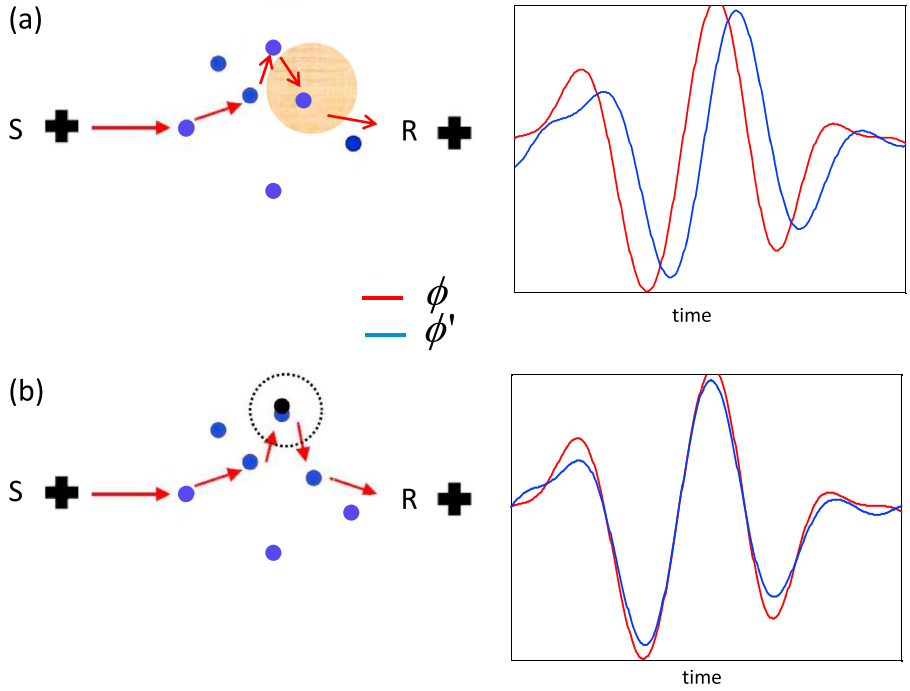


**Figure 3.** Schematic representation of the effect of a (a) weak velocity change and a (b) structural change in the medium on the wave $\Phi'$ (blue) compared to a wave $\Phi$ (red) that has not encountered the change. The weak velocity change causes a phase shift as shown in Figure 3a. The structural change causes waveform decoherence as shown in Figure 3b.

the sedimentary Sichuan basin (SB). Some stations near the epicenter of the earthquake (beach ball in Figure 2) suffered power failure during the main shock; most of them were recovered in the weeks after the quake. Nevertheless, within the small time windows that we study, the data quality degrades increasingly toward the end of 2008.

The available seismic records have been normalized in the time domain. We analyze the vertical component and apply the following further processing steps: (1) resampling of the data to a sampling frequency of 5 Hz, (2) spectral whitening in the period band of 1 s to 3 s and 12 s to 20 s, respectively, (3) application of one-bit normalization, (4) computation of the noise correlations for all of the station pairs with a spacing of <350 km, and (5) stacking of the correlations to obtain a stable cross-correlation function. A difficulty that we face here is the longer the period of the signal, the slower its convergence toward a stable correlation function [e.g., *Larose et al.*, 2007]. We need to stack 50 days in the 1–3 s period band and 100 days in the 12–20 s period band to obtain a stable function, which limits the temporal resolution of our results. We then track the temporal variations in the coda by comparing the current stack, in this case the 50 day/100 day correlation function at each date, to a reference correlation function that is the average over the whole 2 year period. The seismic velocity variations $\delta v/v$ and the waveform coherence CC are computed with the *stretching technique* [*Lobkis and Weaver*, 2003; *Sens-Schönfelder and Wegler*, 2006]. This method is based on the concept that a spatially homogeneous velocity variation in the medium will result in stretching or compression of the waveform (Figure 3a). The stretching method then determines the relative velocity variation $\delta v/v = -\delta t/t$ as the factor $\epsilon$ by which the time axis of the current trace has to be stretched or compressed to obtain the best correlation CC with the reference trace. In case of local medium perturbations, we do not expect a linearly increasing velocity change with increasing time in the coda [*Obermann et al.*, 2013b]. We hence apply the stretching technique to different time windows in the coda (Figure 4). In the 1–3 s period band we use 50 s long windows centered around 30, 50, 70, and 90 s. In the 12–20 s period band we use 90 s long windows (more than two periods) centered around 50, 70, and 90 s in the coda. As the correlation functions are asymmetric (due to an uneven distribution of noise), we perform this analysis on the acausal and causal part of the correlation function and then average the computed delay times and correlation values. We exclude autocorrelations and only work with station pairs that have a coherency value above 0.75 during the background period (neither rainfall nor earthquake disturbances) that is defined in Figure 2d.

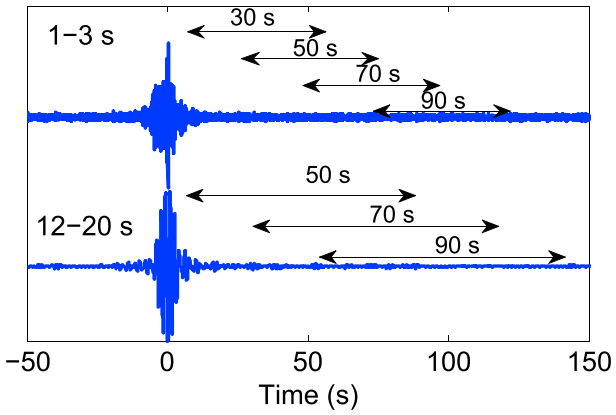


**Figure 4.** Illustration of a reference correlation function for a station pair ≈ 40 km apart in the 1–3 s and 12–20 s period range. We sketch the coda time windows that we use for the inversion. For the 1–3 s period band we use four 50 s long windows centered around 30, 50, 70, and 90 s. In the 12–20 s period band we use 90 s long windows centered around 50, 70, and 90 s.

If the wave did not only encounter a velocity perturbation in the medium but also a structural change of the medium, we observe additional small residual distortions of the waveforms (Figure 3b). To quantify the waveform decoherence DC that has been introduced by the change in the medium, we subtract the current correlation value $CC_i^{Curr}$ of a station pair $i$ from the reference correlation value $CC_i^{Ref}$ that was calculated as the average over the background period (Figure 2d):

$$DC_i = CC_i^{Ref} - CC_i^{Curr}. \quad (1)$$

This waveform decoherence has been used in acoustics on laboratory experiments with aluminum plates [*Michaels and Michaels*, 2005] and on concrete [*Larose et al.*, 2010; *Rossetto et al.*, 2011; *Planès*, 2013] to quantify defects in materials that are much smaller than one wavelength (Locadiff technique). *Obermann et al.* [2013a] used the waveform decoherence successfully to locate preeruptive and coeruptive changes on a volcano with high spatial resolution using ambient seismic noise measurement.

In Figure 2b we show the velocity variations and the waveform coherence with their respective error bars (grey-shaded zones) from early 2007 until late 2008 at 50 s in the coda for the 1–3 s period band (red) and the 12–20 s period band (blue). We here averaged the measurements from the cross correlations in three subregions that are defined in Figure 2a: the Pre-Himalaya (red, I), the Longmen Shan region where the earthquake took place (blue, II), and the southern Sichuan basin (yellow, III). The black dotted line in Figure 2b marks the date of the earthquake. We note that there are no velocity changes or waveform decoherence during the period of interest in the Pre-Himalayan region (I). In the Longmen Shan region (II), we observe a clear velocity drop in the two period bands with onset of the earthquake that reaches its maximum after the earthquake in both frequency bands. In the 12–20 s period band we can further observe a small velocity drop between May and August 2007 that seems to correlate with the accumulated rainfalls during monsoon season in this area (Figure 2c). In the southern Sichuan basin (III), the velocity drop from May to August 2007 is even more pronounced in the 12–20 s period band. In the southern Sichuan basin, we do not observe any significant velocity variations in the 1–3 s period band for the entire period of interest. The coherence in the 12–20 s band remains high (0.95 on average) with only small fluctuations for all three subregions. In the 1–3 s period band, we note a very pronounced decoherence (20%) in July/August 2007 in the Sichuan basin and the Longmen Shan region (II,III). In these regions we also observe a decoherence of about 10% with the onset of the earthquake. The coherence in the 12–20 s period band does not seem to be significantly affected in any region. For the inversion, we define five time periods that we want to study independently and over which we will average the velocity variations and the waveform decoherence measurements for each station pair, respectively. We identify the background state that comprises the parts of the years 2007 and 2008 that are neither affected by the monsoon nor the earthquake: the peak of the monsoon period from June to July 2007, the period centered around May 2008 that includes the earthquake (coseismic), the period from June to July 2008 shortly after the earthquake (postseismic), and the peak of the monsoon season from July to August 2008. The periods are roughly sketched in Figure 2d.

The observations that we made for the velocity variations are, in general, consistent with the observations of *Chen et al.* [2010] and *Froment et al.* [2013]. The slight differences that are there arise mainly from a different selection of station pairs for the subregions. Here we see one of the main interests of the inversion procedure that takes into account the information from all station pairs without averaging them spatially.

Seasonal noise source changes in the ocean have been suggested to be at the origin of velocity changes observed in this region [*Liu et al.*, 2010]. As these changes should affect the entire region in the same

way, which is not the case, we exclude seasonal noise source changes as origin of observed waveform decoherence and velocity variations and relate them solely to changes in the ground.

## 3. Joint Inversion at Different Times in the Coda

The velocity changes measured on noise correlations are representative of changes in a set of scattering paths between two stations. This measure can be viewed as a linear sum of contributions from each space element in the medium. Note that we consider here a two-dimensional medium, as the use of surface waves in a limited period band makes it possible to assume as a first approximation that we are investigating the medium at a specific depth. We hence attempt to locate the velocity changes and the structural changes in the *x*-*y* plane in the shallow and middle crust. We have velocity change ($\varepsilon_i$) and decoherence measurements $DC_i = CC_i^{ref} - CC_i^{curr}$ that correspond to a pair of seismic stations *i*. As these measurements are performed on multiply scattered coda waves that follow very complex paths between the two stations, it is not possible to associate a specific arrival time in the seismograms to a specific trajectory in the medium. The challenge is thus to relate a measurement corresponding to a station pair to every space element of the medium sampled by the coda waves. To do that, it is relevant to describe the wave propagation with probabilities (random walk). We can then compute sensitivity kernels between the stations and apply a linear least squares inversion scheme to locate the changes in the *x*-*y* plane. *Obermann et al.* [2013a] used this inversion scheme with sensitivity kernels in the radiative transfer approximation to locate changes on a volcano. While they use one large time window in the coda for their analysis, we here take several short windows at different times in the coda and invert them simultaneously. By doing so, we expect an increase in resolution and additional information about the depth of the changes [*Obermann et al.*, 2013b].

### 3.1. Sensitivity Kernel

The probabilistic wave propagation in the multiple scattering regime is calculated using the solution to the radiative transfer equation (Boltzmann transport equation). In 2-D for isotropic scattering, the solution reads [*Shang and Gao*, 1988; *Sato*, 1993; *Paasschens*, 1997]

$$p(r,t) = \frac{e^{-ct/\ell}}{2\pi r}\delta(ct-r) + \frac{1}{2\pi\ell ct}\left(1-\frac{r^2}{c^2t^2}\right)^{-\frac{1}{2}} \exp^{[\ell^{-1}(\sqrt{c^2t^2-r^2}-ct)]}\Theta(ct-r), \tag{2}$$

where *c* is the wave speed, *r* is the distance between source and receiver, $\ell$ is the transport mean free path, and $\Theta(x)$ is the Heaviside (or step) function. The first term describes the coherent part of the intensity that decreases exponentially with the distance relative to the transport mean free path. The second term describes the diffuse intensity. We note that the diffusion solution is reached when $t \gg r/c$. With this intensity propagator, we can describe the probability that the wave has traveled between two points in the medium during time *t*. We can now relate the measured velocity changes $\varepsilon_i$ or decoherence measurements $CC_i$ to a local medium perturbation in $x_0$ using the sensitivity kernel introduced by *Pacheco and Snieder* [2005], *Larose et al.* [2010], and *Planès et al.* [2014]:

$$K(\mathbf{s_1},\mathbf{s_2},\mathbf{x_0},t) = \frac{\int_0^t p(\mathbf{s_1},\mathbf{x}_0,u)p(\mathbf{x}_0,\mathbf{s_2},t-u)\mathrm{d}u}{p(\mathbf{s_1},\mathbf{s_2},t)} \tag{3}$$

where $\mathbf{s_1}$ and $\mathbf{s_2}$ are the positions of the stations, $\mathbf{x}_0$ is the position of the local medium perturbation (velocity perturbation or structural change), and *t* is the center of the time interval in the coda where the stretching is evaluated. The intensity propagator in the radiative transfer solution (equation (2)) is $p(s_1, s_2, t)$. The sensitivity kernel is herewith a measure of the statistical time spent in each part of the region at test. An example of the sensitivity kernel *K* is shown in Figure 5a, for very early times in the coda ($t \approx \Delta/v$), compared to the interstation distance $\Delta$, and in Figure 5b for later times ($t > \Delta/v$). We notice that at early times, the waves only sampled a small area along the direct trajectory between the stations, while at later times they became sensitive to a much larger region.

The diffusivity *D* is computed for a velocity $v = 3$ km/s (Rayleigh wave group velocity measured in the 1–3 s period range) and $v = 5$ km/s in the 12–20 s period range. The value of the transport mean free path $\ell$ is difficult to estimate. *Obermann et al.* [2013a] tested the sensitivity of the inversion toward different values of $\ell$ and observed that $\ell$ has an influence on the size of the affected area but not on the location itself. The results presented in the main body of the text correspond to a transport mean free path $\ell$ of 60 km in the 1–3 s period range and 500 km in the 12–20 s period range.

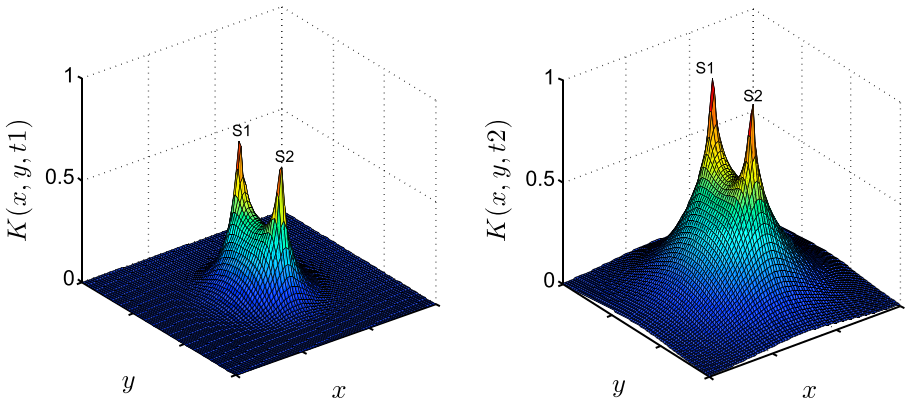


**Figure 5.** Spatial representation of exemplary sensitivity kernels *K* (equation (3)) for station pair *S*1 and *S*2; (a) very early in the coda when the waves just had time to travel between the stations, *t*1 and (b) at a much later time, *t*2. The values along the vertical axis can be interpreted as the sensitivity toward a perturbation in the medium located in (*x*, *y*).

### 3.2. Linear Least Squares Inversion at Different Times in the Coda

To estimate the horizontal distribution of the changes in the study area, we pose the forward problem in form of a system of linear equations in matrix form according to

$$\mathbf{d} = \mathbf{Gm}, \tag{4}$$

where **d** is a vector, for which each component $d_i (i = 1...n)$ corresponds to the apparent velocity change or decoherence that we measured for a given station pair and time in the coda with the stretching technique; *n* is the total number of measurements; **G** is a matrix, for which each component $G_{ij}$ corresponds to the sensitivity kernel *K* for station pair *i* in cell *j* evaluated at time $t_i$ in the coda and weighted by the surface of the cells $\Delta s$ and either the lapse time $t_i$ in the coda (velocity changes) or the Rayleigh wave group velocity *c* (decoherence measurements); and **m** is a vector, for which each component $m_j$ contains the actual relative velocity changes that we estimate for each pixel *j* (without units) or the scattering cross-section density change $\sigma$ (km/km$^2$):

$$d_i = \varepsilon_i, G_{ij} = \frac{\Delta s}{t} K_{ij}, m_j = \frac{\delta v}{v}_j. \tag{5}$$

$$d_i = \mathrm{DC}_i, G_{ij} = \frac{c\Delta s}{2} K_{ij}, m_j = \sigma_j. \tag{6}$$

When the data that we invert represent local velocity changes, there is no constraint concerning the sign of **m**. We can thus directly use the formulation of the linear least squares method as proposed by *Tarantola and Valette* [1982] to determine **m**:

$$\boldsymbol{m} = \boldsymbol{m}_0 + \boldsymbol{C}_m \boldsymbol{G}^t (\boldsymbol{G}\boldsymbol{C}_m \boldsymbol{G}^t + \boldsymbol{C}_d)^{-1} (\boldsymbol{\varepsilon} - \boldsymbol{G}\boldsymbol{m}_0), \tag{7}$$

where $\boldsymbol{m}_0$ is the a priori model, a zero vector in our case, as we do not possess any a priori information about the expected changes. $\boldsymbol{C}_d$ is the diagonal covariance matrix for the data and contains the variances of the data $\mathrm{std}_{d,i}^2$. To estimate the standard deviation $\mathrm{std}_{d,i}$ of the data, we use the theoretical formulation proposed by *Weaver et al.* [2011]:

$$\mathrm{std}_{d,i} = \frac{\sqrt{1 - \mathrm{CC}_i^2}}{2\mathrm{CC}_i} \sqrt{\frac{6\sqrt{\frac{\pi}{2}}T}{\omega_c^2 (t_2^3 - t_1^3)}}. \tag{8}$$

*T* is the inverse of the central frequency in one of the bands, $t_1$ and $t_2$ are the begin and end of the processed time window in the coda, $\omega_c = 2\pi f_c$ is the central angular frequency ($f_c$ is the central frequency), and $\mathrm{CC}_i = \mathrm{CC}(\varepsilon_i)$ is the coherence value of the respective station couple *i* with a stretching of $\varepsilon_i$.

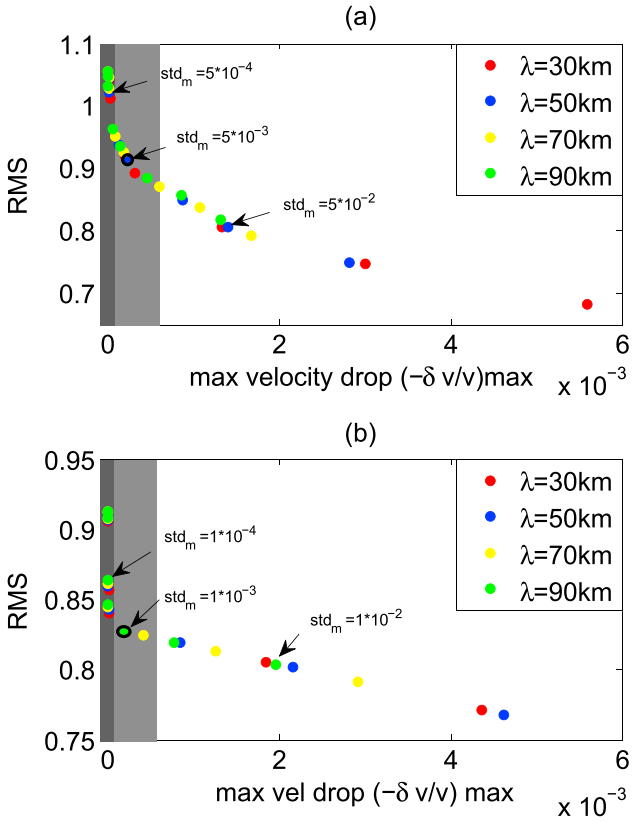


**Figure 6.** *L* curve in (a) the 1–3 s period band and in (b) the 12–20 s period band. The normalized residuals are plotted as a function of maximal velocity fluctuations in the model for different values of the smoothing parameters $\text{std}_m$ and $\lambda$. The background shadings indicate different smoothing regimes. The optimal smoothing parameters are found in the region with maximal bending of the curve (light grey). The parameters chosen are marked with a black circle.

$\boldsymbol{C}_m$ is the nondiagonal covariance matrix of the model that introduces a spatial smoothing:

$$C_{m_{ij}} = \left(\text{std}_m \frac{\lambda_0}{\lambda}\right)^2 \exp\left(-\frac{\Delta_{ij}}{\lambda}\right), \tag{9}$$

where $\Delta_{ij}$ is the distance between two cells $i$ and $j$. The smoothing or correlation length is $\lambda$, and the variance of the model weighted by $\left(\frac{\lambda_0}{\lambda}\right)^2$ is $\text{std}_m^2$, where $\lambda_0$ is a reference scaling length, which is here taken equal to the cell size (20 km). In that way, the damping is related to the smoothing: the longer $\lambda$, the greater the smoothing and damping. The smoothing is of importance as in most cases the inverse problem is underdetermined. We determine the value of these parameters with the help of an *L* curve [*Hansen*, 1992] to get a good trade-off between the data fit and the smoothness of the velocity fluctuations. In Figure 6 we plot the root-mean-square $\left(\text{RMS} = \sqrt{\frac{1}{n}\sum_{i=1}^{n}\frac{(\varepsilon_i - Gm_i)^2}{std_{d,i}}}\right)$ between $n$ measured ($\varepsilon$) and modeled ($Gm$) apparent velocity variations as a function of the maximal velocity fluctuations in the model for different values of $\lambda$ and $\text{std}_m$: for the 1–3 s period band in Figure 6a and for the 12–20 s period band in Figure 6a. The best trade-off parameters approximately correspond to the maximal bending of the curve (light grey). The white zone indicates a too weak smoothing that allows very strong velocity variations in the final model. The dark gray zone indicates a too strong smoothing for which the velocity variations are weak but the data fit is very poor. As trade-off parameters we chose $\text{std}_m = 5 \times 10^{-3}$ and $\lambda = 50$ km for the data in the 1–3 s period band and $\text{std}_m = 1 \times 10^{-3}$ and $\lambda = 90$ km for the data in the 12–20 s period band.

When we study the decoherence, the scattering cross-section density that we obtain is necessarily positive, and we need to impose a positivity constraint during the inversion. We therefore use an iterative procedure. The initial model $m_0$ is again zero everywhere, and then at each iteration step, we only keep positive values and use this model as a new input model. We use eight iterations to obtain the scattering cross-section maps shown in Figure 7.

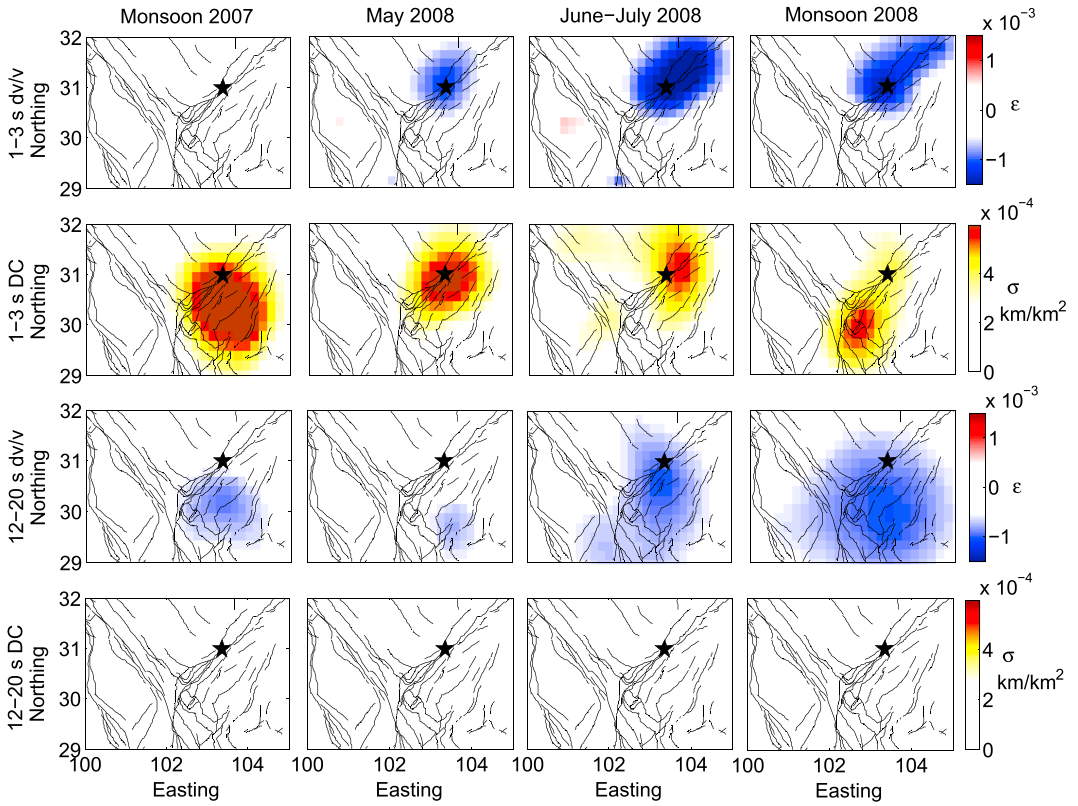


**Figure 7.** Least squares inversion of the relative velocity changes ($\varepsilon$) and the decoherence values (DC) in the 1–3 s (jointly for 30, 50, 70, and 90 s in the coda) and in the 12–20 s period band (jointly for 50, 70, and 90 s in the coda). In the columns we show the results for the different states identified in Figure 2d.

We compute the kernels at different lapse times in the coda and then jointly invert the data. This increases the amount of data and hence better constraints the inversion.

We study an area from 100°E to 105°E and from 29°N to 32°N (Figure 2), which covers a region of about 480 km × 340 km. To minimize model-edge effects across the region of interest, we model the velocity variations in a larger zone. In view of the spreading of the sensitivity kernels used, we have decided to consider the region of interest extended by 250 km in each direction. We finally investigate the changes in 51 × 42 = 2193 cells of 20 km × 20 km ($\Delta S = 400$ km$^2$).

In this monitoring context, the data are available for 65 ted-day periods between January 2007 and October 2008. We focus on five specific periods as shown in Figure 2e. Within each of these periods we average the measured velocity changes and decoherence values. As mentioned previously, we apply a quality criterion and invert only the measurements from station pairs with average correlation coefficients above 0.75 in the background state. This leaves us with about 600 station pair measurements that cover the entire area.

## 4. Inversion Results in the 1–3 s and 12–20 s Period Bands

In this section we discuss the inversion results for the velocity variations and the waveform decoherences in both frequency bands and at different times in the coda. In section 4.1 we then display quality tests that we perform to confirm the validity of our models, but that is not necessary for the interpretation.

In Figure 7 we display the images of the velocity variations based on the inversion of the relative delays in the coda and the images of the structural changes (scattering cross section of the change) based on the inversion of the decoherence values in the coda (first and third rows for the 1–3 s period band and second and fourth rows for the 12–20 s period band). The images are the joint inversion results for different times in the coda as indicated in Figure 4. We display in each column from left to right the averages for the states identified in Figure 2d. We recall that velocity drops indicate mechanical weakening of the material,

while a decoherence indicates structural changes that result from changes of the scattering properties of the medium.

The 2-D horizontal maps with the velocity variations in the 1–3 s period band (Figure 7, first row) show no velocity variation during the monsoon season in 2007, whereas we observe a coseismic velocity drop (−0.8%) at the earthquake location and a strong postseismic signature (−2%) over a large area that includes the aftershocks along the fault zone (red dots in Figure 2). In the monsoon period 2008 we still observe a velocity drop at the earthquake location and along the fault zone.

When studying the 2-D horizontal maps with the scattering cross-section densities (Figure 7, second row), we observe a strong decoherence in the Sichuan basin during the monsoon season 2007. We further observe a coseismic decoherence that affects the area around the earthquake. The postseismic signature is weaker and extends toward the north of the epicenter, along the fault zone with the aftershocks. In the monsoon period 2008 we observe a small decoherence at the earthquake location and a strong, localized decoherence in the Sichuan basin.

When studying the velocity variations in the 12–20 s period band (Figure 7, third row), we observe a velocity drop in the Sichuan basin during the monsoon period 2007. We observe a very local, low-amplitude, velocity drop in the Sichuan basin during the coseismic period but no visible velocity variations at the earthquake location. In the period from June to July 2008, we observe velocity drops in the entire Sichuan basin including the earthquake zone and extending in the Songpan-Ganzi. During the peak of the monsoon period in 2008, we observe an extended velocity drop in the Sichuan basin extending in the Songpan-Ganzi.

In the 12–20 s period band (Figure 7, fourth row) we do not observe a significant decoherence for any of the states.

These observations lead us to propose interpretations concerning the effect of the rain and of the earthquake on the velocity variations and the waveform decoherence. Let us start with the observations during the monsoon periods of 2007 and 2008. The changes of the water table in the Sichuan basin during the monsoon (Figure 2) can be seen in form of a decoherence in the 1–3 s period band and as a velocity drop in the 12–20 s period band, whereas we do not observe a significant velocity drop in the 1–3 s period band. The Sichuan basin is saturated all year long. The additional rain seems to have very local effects (change in river load, flooding, etc.) that are not detectable as a modification of the elastic parameters at large scale, but that contribute to a significant waveform decoherence. At depth (12–20 s), we follow the interpretation from *Froment et al.* [2013] that it is the loading due to the rain that induces a significant deformation but not the water saturation itself. The loading can significantly increase the pore pressure [*Bettinelli et al.*, 2008] and hence cause a velocity diminution [*Dvorkin et al.*, 1999; *Carcione and Tinivella*, 2001]. Another strong lead in this direction is the remarkable synchrony of the rain and the velocity drop. This excludes that fluid transport at depth could be at its origin, as the hydrological diffusion time would delay the response. It indicates more instantaneous mechanical effects that go in hand with the interpretation of the velocity drop as a consequence of the loading. The absence of the signal in the 1–3 s period band excludes seasonal thermoelastic effects that should be strong close to the surface. We also exclude seasonal changes of the noise sources to be at the origin of the observed changes, as in this case we could expect the entire region to be affected, whereas we observe a localization of the changes.

The coseismic and postseismic observations suggest the following interpretations. The coseismic signature (velocity drop and decoherence) in the 1–3 s period band around the earthquake epicenter can be directly related to the strong damages caused by the earthquake at the surface and in the fault zone itself (240 km long rupture zone, up to 10 m vertical offset, numerous landslides). The strong postseismic velocity drop along the fault zone is occurring in the region where most of the aftershocks occurred. It is possible that it is associated with the nonlinear dynamic response of the shallow layers to the numerous aftershocks. The nonlinear response of shallow layers to strong motion has been observed to have a rapid recovery [*Sawazaki et al.*, 2006; *Karabulut and Bouchon*, 2007; *Rubinstein et al.*, 2007]. In the 12–20 s period band, we do not observe a significant coseismic signature. This could indicate that the nonlinear effects due to the strong motions are limited to the surface. Instead, we observe a significant postseismic change at the earthquake location that extends in the Songpan-Ganzi north of the fault and into the Sichuan basin. To interpret these changes at depth, we have a look at the evolution of the changes with lapse time in the coda.

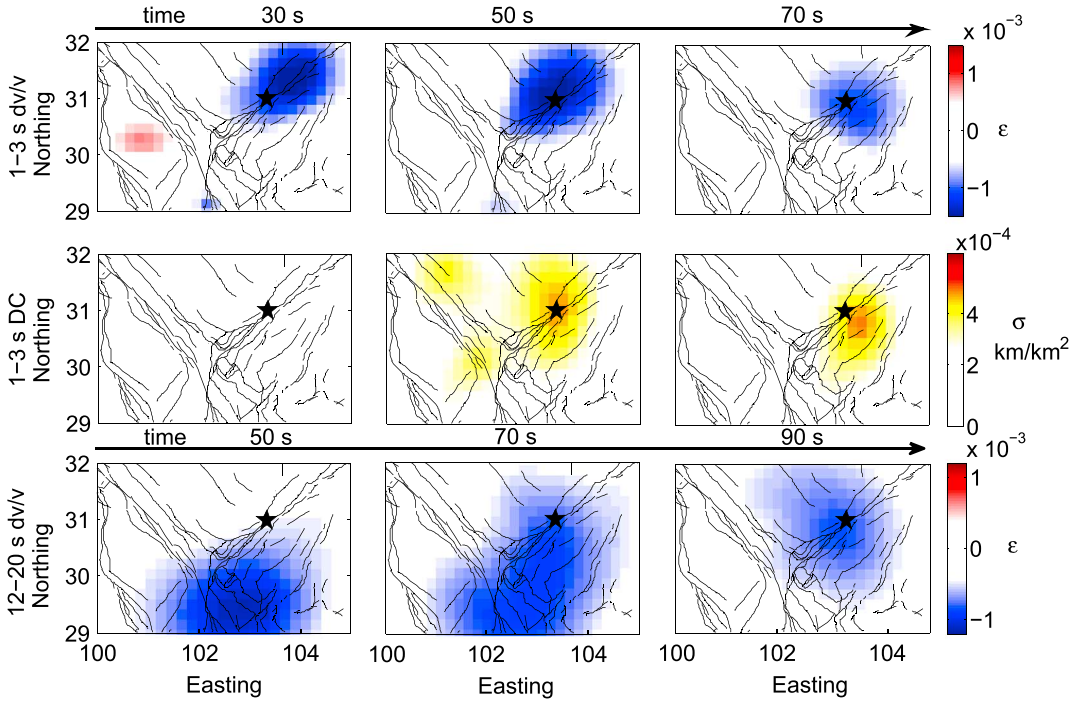


**Figure 8.** Evolution of the velocity $\varepsilon$ and the decoherence DC changes after the earthquake (June–July 2008) in the 1–3 s period band at 30, 50, and 70 s in the coda and $dv/v$ in the 12–20 s period band at 50, 70, and 90 s in the coda.

Please note that since our measurements correspond to both space and time average, the overall amplitude of the changes should not be overinterpreted.

In Figure 8 we focus on the evolution of the changes with lapse time in the coda during the postseismic period in both frequency bands. We here invert the velocity variations and the waveform decoherences at each time in the coda separately. *Obermann et al.* [2013b] have shown based on scattering and mode conversion arguments that surface waves statistically dominate the early part of a seismic record, whereas bulk waves play an increasingly important role in the later part. As a consequence, changes at shallow depth (compared to the wavelength) result in a large-amplitude velocity change (or decoherence) at early lapse times and then decrease in amplitude later. On the contrary, for changes at depths greater than the wavelength, the velocity change will increase from a negligible value at early times to a significant contribution at later times. With this analysis, we hence expect to obtain some additional information about the nature of the changes, especially at depth. We notice that the velocity drop in the 1–3 s period band is stronger at early times in the coda (30 s) than at later times (50 and 70 s). The decoherence in this period band shows the opposite behavior; there is no decoherence at early times, while it grows larger at later times in the coda. We hence conclude that the mechanical changes occurred within one wavelength from the surface, while the structural changes also took place further at depth.

In the 12–20 s period we observe a velocity drop in the Sichuan basin at early times in the coda (50 s), whereas the sensitivity shifts toward the earthquake location at later times (70 and 90 s). In this period band, the coda is dominated at early times by scattered surface waves that have their highest sensitivity down to about 20 km (Figure 1). We hence conclude that the loading due to the monsoon mainly affects the upper 20 km of the crust. At later lapse times the significant contribution of body waves in the coda [*Obermann et al.*, 2013b] allows to sample much deeper regions. The velocity drop that we observe at these times is distinct at the earthquake location and north of the Longmen Shan fault. This indicates that the earthquake caused a significant change of the mechanical parameters at depth. The location of the velocity decrease is in agreement with the observations from *Cheng et al.* [2010] who report changes in seismic velocity due to the earthquake in an elongated area in the northwest of the Longmen Shan fault at comparable periods of 10 to 25 s. As a cause of these changes at depth, we have to consider the possible influence of the detachment of a deep fault segment beneath eastern Tibet in relation to the Wenchuan earthquake that has been

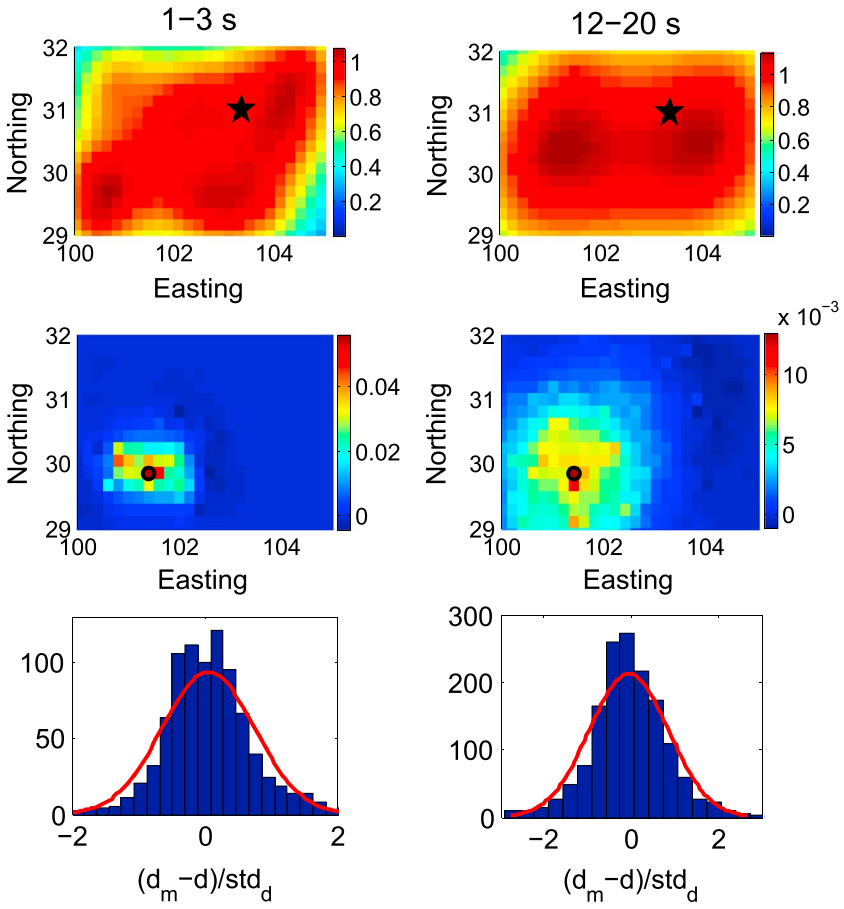


**Figure 9.** Quality tests for (left) the 1–3 s period band and (right) the 12–20 s period band. (first row) Model resolution in the area of interest. The star denotes the epicenter location. (second row) Resolution for the cell indicated with an open circle. (third row) In blue, the distribution of the standard deviation between the modeled and measured apparent velocity variations. The red curve corresponds to a Gaussian distribution and indicates that the residuals are well described by a normal distribution.

proposed by *Fielding et al.* [2013] in an extensive synthetic aperture radar interferometry, GPS, and teleseismic analysis. Although the timing of the deep deformation and the partition between post seismic slip and viscoelastic response of the deep crust remain uncertain, the extension of the tectonic process at depth beneath Tibet is likely.

### 4.1. Quality Tests of the Inversion Model

To confirm the efficiency of the inversion result, we consider the model resolution. The resolution operator is defined as

$$\boldsymbol{R} = \boldsymbol{C}_m \boldsymbol{G}^t (\boldsymbol{G}\boldsymbol{C}_m \boldsymbol{G}^t + \boldsymbol{C}_d)^{-1} \boldsymbol{G} = \boldsymbol{I} - (\boldsymbol{C}_m^{-1} + \boldsymbol{G}^t \boldsymbol{C}_d^{-1} \boldsymbol{G})^{-1} \boldsymbol{C}_m^{-1}, \tag{10}$$

denoting by $I$ the identity in the model space. $R$ relates the resulting model correction $\mathbf{m} - \mathbf{m}_0$ to the true model correction $\boldsymbol{m}_t - \boldsymbol{m}_0$ according to, e.g., *Tarantola and Valette* [1982]:

$$\boldsymbol{m} - \boldsymbol{m}_0 = \boldsymbol{R}(\boldsymbol{m}_t - \boldsymbol{m}_0) + \text{noise}, \tag{11}$$

where the *noise* term comes from the discrepancy between true and observed data.

Of particular interest is the averaging index [*Vergely et al.*, 2010] which, given a cell $i$, is defined as the sum of the coefficients $R_{ij}$ of the line $i$ in the resolution matrix. In those areas (cells $i$) were the data provide poor information, the averaging index is very low, indicating that the resulting value $m_i$ of the model at cell $i$ remains close to the prior 1 $m_{0i}$, independently of the true model in the neighborhood. But, when the averaging index is close to 1, the resulting value of the model approximately corresponds to a spatial average

of the true model. In the first row of Figure 9 we display the averaging indexes for both frequency bands for the region of interest, indicating the limits of the zone where the inference becomes poor (below 0.7, only close to the borders). Within these limits of inference, the spread of the resolution must be evaluated for a complete set of points (cells) in order to appreciate correctly the resolution.

In the second row of Figure 9 we display the resolution for a representative cell *i* of the set (i.e., the *i*th line of the matrix *R*), again for both frequency bands. The chosen cell is marked with an empty circle and well situated in the zone were the model predicts the maximal velocity variations. The figure shows that the resolution spread is smaller for the 1–3 s period band (about 40 km) than for the 12–20 s one (about 70 km), in accordance with the prior choice for the correlation lengths $\lambda$.

In the third row of Figure 9 we show for both frequency bands the distribution of the standard deviation between the measured $\epsilon$ and modeled $\epsilon_{\mathrm{mod}}$ velocity variations, normalized with the characteristic error of the data. They are well fitted with a Gaussian distribution (red curve).

## 5. Conclusion

In the present study, we investigated the temporal evolution of elastic and scattering parameters in the crust at different depth ranging from 0 to 40 km over 2 years including the 12 May 2008 $M_w$ 7.9 Wenchuan earthquake. We monitored the temporal evolution by measuring seismic velocity changes and also waveform decoherence in the coda part of the noise correlation functions. We could detect coseismic and postseismic changes, as well as changes associated with the monsoon seasons. We studied the spatial distribution of these temporal changes with a refined localization method that is based on the inversion of the velocity change/waveform decoherence measurements at different times in the coda. With both measurements, we could locate the damage around the earthquake epicenter and along the rupture zone. We also observed that the crust below the hypocenter suffered from significant postseismic changes in its elastic parameters that could be due to slow transfer of the load caused by the earthquake (poroelastic relaxation).

We could further see a significant loading effect from the rain during the monsoon season on the middle crust in form of the velocity drop. This hydrological change is also visible close to the surface in form of a waveform decoherence introduced by the changes in scattering properties probably due to river activity/level. We observed that the two observables, apparent velocity change (phase of the seismic signal) and waveform decoherence (waveform of the seismic signal), are not sensitive to the same physical parameters. They must have different physical origins. Velocity changes are associated with changes in the poroelasticity of the medium, while waveform decoherence is associated with changes in the scattering properties of the medium (structural changes). We emphasize the importance of simultaneously studying velocity variations and waveform decoherence to increase the efficiency of ambient noise monitoring.

**Acknowledgments**
This study is part of the ERC Advanced grant Whisper 227507. We thank Xavier Briand for his outstanding and timely computational assistance that underpinned much of this work. We acknowledge the excellent review of Elmer Ruigrok and an anonymous reviewer, which were of great help toward the improvement of our manuscript.

## References

Bettinelli, P., J. P. Avouac, M. Flouzat, L. Bollinger, G. Ramillien, S. Rajaure, and S. Sapkota (2008), Seasonal variations of seismicity and geodetic strain in the Himalaya induced by surface hydrology, *Earth Planet. Sci. Lett.*, 266–344.

Brenguier, F., M. Campillo, C. Hadziioannou, N. M. Shapiro, R. M. Nadeau, and E. Larose (2008), Postseismic relaxation along the San Andreas Fault at Parkfield from continuous seismological observations, *Science*, *321*, 1478–1481.

Burchfiel, B. C., L. H. Royden, R. D. van der Hilst, Z. Chen, R. W. King, C. Li, J. Lu, H. Yao, and E. Kirby (2008), A geological and geophysical context for the Wenchuan earthquake of 12 May 2008, Sichuan, People's Republic of China, *GSA Today*, *18*(7), 4–11.

Carcione, J. M., and U. Tinivella (2001), The seismic response to overpressure: A modelling study based on laboratory, well and seismic data, *Geophys. Prospect.*, *49*, 523–539.

Chen, J. H., Q. Y. Liu, S. C. Li, B. Guo, J. Wang, and S. H. Qi (2009), Seismotectonic study by relocation of the Wenchuan $M_S$8.0 earthquake sequence, *Chinese J. Geophys.*, *52*(2), 390–397.

Chen, J. H., B. Froment, Q. Y. Liu, and M. Campillo (2010), Distribution of seismic wave speed changes associated with the 12 May 2008 Mw 7.9 Wenchuan earthquake, *Geophys. Res. Lett.*, *37*, L18302, doi:10.1029/2010GL044582.

Cheng, X., F. Niu, and B. Wang (2010), Coseismic velocity change in the rupture zone of the 2008 Mw 7.9 Wenchuan earthquake observed from ambient seismic noise, *Bull. Seismol. Soc. Am.*, *100*(5B), 2539–2550.

Dvorkin, J., G. Mavko, and A. Nur (1999), Overpressure detection from compressional-and shear-wave data, *Geophys. Res. Lett.*, *26*(22), 3417–3420.

Fielding, E., A. Sladen, Z. Li, J. P. Avouac, R. Bürgmann, and I. Ryder (2013), Kinematic fault slip evolution source models of the 2008 Mw7.0 Wenchuan earthquake in China from SAR interferometry, GPS and teleseismic analysis and implications for the Longmen Shan tectonics, *Geophys. J. Int.*, *194*, 1138–1166, doi:10.1093/gji/ggt155.

Froment, B. (2011), Utilisation du bruit sismique ambiant dans le suivi temporel de structures géologiques, PhD thesis, Université de Grenoble, Grenoble, France.

Froment, B., M. Campillo, J. H. Chen, and Q. Y. Liu (2013), Deformation at depth associated with the May 12, 2008 Mw 7.9 Wenchuan earthquake from seismic ambient noise monitoring, *Geophys. Res. Lett.*, *40*, 78–82, doi:10.1029/2012GL053995.

Fu, B., P. Shi, H. Guo, S. Okuyama, Y. Ninomiya, and S. Wright (2011), Surface deformation related to the 2008 Wenchuan earthquake, and mountain building of the Longmen Shan, eastern Tibetan Plateau, *J. Asian Earth Sci.*, *40*, 805–824.

Hansen, P. C. (1992), Analysis of discrete ill-posed problems by means of the L-curve, *SIAM Rev.*, *34*(4), 561–580.

Karabulut, H., and H. Bouchon (2007), Spatial variability and non-linearity of strong ground motion near a fault, *Geophys. J. Int.*, *170*, 262–274.

Larose, E., P. Roux, and M. Campillo (2007), Reconstruction of Rayleigh-Lamb dispersion spectrum based on noise obtained from an air-jet forcing, *J. Acous. Soc. Am.*, *122*(6), 3437–3444.

Larose, E., T. Planès, V. Rossetto, and L. Margerin (2010), Locating a small change in a multiple scattering environment, *Appl. Phys. Lett.*, *96*(20), 204,101, doi:10.1063/1.3431269.

Liu, Z. K., J. L. Huang, and J. J. Li (2010), Comparison of four techniques for estimating temporal change of seismic velocity with passive image interferometry, *Earthq. Sci.*, *23*, 511–518.

Lobkis, O. I., and R. L. Weaver (2003), Coda-wave interferometry in finite solids: Recovery of P-to-S conversion rates in an elastodynamic billiard, *Phys. Rev. Lett.*, *90*(25), 254,302, doi:10.1103/PhysRevLett.90.254302.

Michaels, J. E., and T. E. Michaels (2005), Detection of structural damage from the local temporal coherence of diffuse ultrasonic signals, *IEEE Trans. Ultrason. Ferroelectr. Freq. Control*, *52*(10), 1769–1782.

Obermann, A., T. Planès, E. Larose, and M. Campillo (2013a), Imaging pre- and co-eruptive structural and mechanical changes on a volcano with ambient seismic noise, *J. Geophys. Res. Solid Earth*, *118*, 6285–6294, doi:10.1002/2013JB010399.

Obermann, A., T. Planès, E. Larose, C. Sens-Schönfelder, and M. Campillo (2013b), Depth sensitivity of seismic coda waves to velocity perturbations in an elastic heterogeneous medium, *Geophys. J. Int.*, *194*(1), 372–382.

Paasschens, J. C. J. (1997), Solution of the time-dependent Boltzmann equation, *Phys. Rev. E*, *56*(1), 1135, doi:10.1103/PhysRevE.56.1135.

Pacheco, C., and R. Snieder (2005), Time-lapse travel time change of multiply scattered acoustic waves, *J. Acoust. Soc. Am.*, *118*, 1300–1310.

Planès, T. (2013), Imagerie de changements locaux en régime de diffusion multiple, PhD thesis, Université de Grenoble, Grenoble, France.

Planès, T., E. Larose, L. Margerin, V. Rossetto, and C. Sens-Schönfelder (2014), Decorrelation and phase-shift of coda waves induced by local changes: Multiple scattering approach and numerical validation, *Waves Random Complex*, doi:10.1080/17455030.2014.880821.

Rossetto, V., L. Margerin, T. Planès, and E. Larose (2011), Locating a weak change using diffuse waves: Theoretical approach and inversion procedure, *J. Appl. Phys.*, *109*(3), 034,903, doi:10.1063/1.3544503.

Rubinstein, J. L., N. Uchida, and G. C. Beroza (2007), Seismic velocity reductions caused by the 2003 Tokachi-Oki earthquake, *J. Geophys. Res.*, *112*, B05315, doi:10.1029/2006JB004440.

Sato, H. (1993), Energy transportation in one- and two-dimensional scattering media: Analytic solutions of the multiple isotropic scattering model, *Geophys. J. Int.*, *112*, 141–146.

Sawazaki, K., H. Sato, H. Nakahara, and T. Nishimura (2006), Temporal change in site response caused by earthquake strong motion as revealed from coda spectral ratio measurement, *Geophys. Res. Lett.*, *33*, L21303, doi:10.1029/2006GL027938.

Sens-Schönfelder, C., and U. Wegler (2006), Passive image interferometry and seasonal variations of seismic velocities at Merapi Volcano, Indonesia, *Geophys. Res. Lett.*, *33*, L21302, doi:10.1029/2006GL027797.

Shang, T., and L. Gao (1988), Transportation theory of multiple scattering and its application to seismic coda waves of impulsive source, *Sci. Sinica*, *31*, 1503–1514.

Stehly, L., M. Campillo, and N. M. Shapiro (2007), Travel-time measurements from noise correlation: Stability and detection of instrumental time-shifts, *Geophys. J. Int.*, *171*(1), 220–230.

Tarantola, A., and B. Valette (1982), Generalized nonlinear inverse problems solved using the least squares criterion, *Rev. Geophys.*, *20*(2), 219–232.

Vergely, J. L., B. Valette, R. Lallement, and S. Raimond (2010), Spatial distribution of interstellar dust in the sun's vicinity - comparison with neutral sodium-bearing gas, *Astron. Astrophys.*, *518*, A31, doi:10.1051/0004-6361/200913962.

Weaver, R. L., C. Hadziioannou, E. Larose, and M. Campillo (2011), On the precision of noise correlation interferometry, *Geophys. J. Int.*, *185*(3), 1384–1392.

Xu, X. W., X. Z. Wen, G. H. Yu, G. H. Chen, Y. Klinger, J. Hubbard, and J. Shaw (2009), Coseismic reverse- and oblique-slip surface faulting generated by the 2008 Mw 7.9 Wenchuan earthquake, China, *Geology*, *37*(6), 515–518.

Zhang, P. Z., X. Z. Wen, Z. K. Shen, and J. H. Chen (2010), Oblique, high-angle, listric-reverse faulting and associated development of strain: The Wenchuan earthquake of May 12, 2008, Sichuan, China, *Annu. Rev. Earth Planet. Sci.*, *38*, 353–382.